Lab-on-a-tissue : optimization of on-tissue chemistry for improved mass spectrometry imaging

Heijs, B.P.A.M.

Chapter 6

Mass spectrometry imaging of *N*-glycans identifies biomarkers of tumor progression in myxoid liposarcoma

Bram Heijs; Stephanie Holst; Inge H. Briaire-de Bruijn; Manfred Wuhrer; Judith V.M.G. Bovée; Liam A. McDonnell, *in preparation*, 2017

Myxoid liposarcoma (MLS) is the second most common subtype of liposarcoma, accounting for approximately 6% of all sarcoma cases. MLS is characterized by a myxoid extracellular matrix and, in 95% of the cases, by the chromosomal translocation t(12;16)(q13;p11), which results in the FUS-DDIT3 chimeric gene. The presence of >5% round cells in MLS is associated with a poorer prognosis for the patient, along with other risk factors like the presence of necrosis, increased tumor size, increased age, and the male gender. While activation of PI3K/Akt signaling and overexpression of microRNA miR-135b have been associated with tumor progression in MLS, the molecular mechanisms underlying the disease progression are largely unknown. Here we have applied matrix-assisted laser desorption/ionization mass spectrometry imaging (MALDI-MSI), an analytical technique capable of simultaneously recording the spatial distributions of hundreds of biomolecules directly from a tissue section, to analyze N-linked glycans from a MLS tissue microarray in order to identify molecular markers for MLS tumor progression. Comparison of the N-glycan profiles revealed that several high-mannose type glycans, and a monofucosylated, triantennary complex-type glycan were associated with tumor progression, and which mirror recent observations in colorectal cancer, breast cancer, and ovarian cancer.

6.1 Introduction

Liposarcomas (LPS) are mesenchymal neoplasms displaying variable levels of adipogenic differentiation. Liposarcoma has a yearly incidence of approximately 30 cases per million, and represents 17-25% of all sarcoma cases (Fletcher et al., 2013; Lemeur et al., 2015). The World Health Organization (WHO) classification describes four different LPS subtypes: (i) well-differentiated, (ii) dedifferentiated, (iii) pleomorphic, and (iv) myxoid (Fletcher et al., 2013). Myxoid liposarcoma (MLS) is the second most common subtype of LPS, accounting for approximately 30% of all LPS cases and 6% of all sarcoma cases (Nishida et al., 2010). MLS is characterized by a myxoid extracellular matrix (ECM) and, in over 95% of cases, by the chromosomal translocation t(12;16)(q13;p11), which results in the chimeric FUS-DDIT3 gene. MLS commonly occurs in the extremities of patients that are typically of a younger age compared to other LPS subtypes (Fletcher et al., 2013). The presence of >5% round cells in MLS is associated with a poorer prognosis, as are the presence of necrosis, increased tumor size (>10 cm), increased age (> 45 years), and the male gender. The treatment of MLS is fairly effective; nonetheless 35-50% will develop either recurrence or metastasis. Treatment includes surgical excision, or a combination of chemo- and/or radiotherapy with surgical excision. Grading of MLS is done by histological examination of the MLS tissue, and depends on the extent of the round cell component in the tissue: <5% round cell component equals a low grade MLS, and ≥5% round cell component defines high grade MLS cases (previously designated as round cell liposarcoma) (Fletcher et al., 2013; de Graaff et al., 2016; Lemeur et al., 2015; Nishida et al., 2010). High intra-tumor heterogeneity may complicate the determination of histological grade, especially when the tumor mass is poorly represented by a small

biopsy (Fritchie et al., 2012). While it is widely accepted that the presence of the round cells is associated with a poor prognosis and higher risk of metastasis, the underlying molecular mechanisms of tumor progression are largely unknown. In a previous immunohistochemistry (IHC) –based study by Demicco *et al.* the progression of MLS was shown to be accompanied by activation of the PI3K/Akt pathway caused by overexpression of insulin-like growth factor 1 receptor (IGF1R), a loss of phosphatase and tensin homolog (PTEN), and activating mutations in phosphatidylinositol 4,5-bisphosphate 3-kinase catalytic subunit alpha isoform (PIK3CA) (Demicco et al., 2011). A more recent report by Nezu *et al.* shows that the overexpression of microRNA miR-135b in MLS results in down regulation of the THBS2 gene, coding for the glycoprotein thrombospondin-2 (TSP2), which in its turn increases expression of matrix metalloproteinase 2 (MMP2), responsible for enhanced degradation of the ECM and ultimately results in increased MLS aggressiveness (Nezu et al., 2016).

Conventional omics-analyses (e.g. genomics, transcriptomics, proteomics) have had limited success in MLS due to its high degree of intra-tumor heterogeneity. Nezu *et al.* used laser-capture microdissection to separate the contributions from the different cell-types present in MLS (Nezu et al., 2016). This result strongly indicates the need for histopathological specification for any investigation of the molecular changes associated with MLS.

Matrix-assisted laser desorption/ionization mass spectrometry imaging (MALDI-MSI) is an analytical technique that allows the spatially-correlated molecular analysis of various molecular classes directly from tissue (Caprioli et al., 1997; McDonnell and Heeren, 2007). By combining the molecular analysis of modern biomolecular mass spectrometry with the imaging capabilities of microscopy MALDI-MSI enables the spatial distributions of 100's to 1000's of biomolecules to be simultaneously recorded without labeling and is untargeted in nature. Furthermore, MALDI-MSI does not adversely affect the tissue's underlying histology; consequently, the tissue may be histologically stained after the MSI experiment and the histological image aligned with the MSI dataset. This multimodal data, MSI and histology, allows the tissue's molecular content to be examined in its correct histopathological context, and thus, for instance, to compare low and high grade areas within a single tissue section. In a process termed virtual microdissection cell-type specific molecular signatures can be extracted, and then used to identify biomarkers (Balluff et al., 2015; Elsner et al., 2012; Lou et al., 2016; Meding et al., 2012).

MALDI-MSI can be used to analyze different molecular classes, using essentially the same technology but different tissue preparation procedures. On-tissue digestion MALDI-MSI using proteolytic enzymes is used to increase the range of proteins amenable to MALDI-MSI analysis, aid their identification and allows the analysis of formalin-fixed, paraffin-embedded (FFPE) tissues (Gustafsson et al., 2013; Heijs et al., 2015; Kriegsmann et al., 2016; Schober et al., 2011). On-tissue digestion MALDI-MSI

using the endoglycosidase PNGase F enables the analysis of *N*-linked glycans, also from both fresh frozen and FFPE tissue sections (Powers et al., 2013, 2015). Proteins, previously associated with MLS tumor progression, such as TSP2, IGF1R, and other receptor tyrosine kinases, involved in the activation of the PIK3/Akt pathway, are known glycoproteins (Carlson et al., 2005; Itkonen and Mills, 2015; Negri et al., 2010). While these proteins have a known role in MLS progression, the role of the *N*-glycans is unknown. Therefore, we have analyzed the *N*-glycans by on-tissue digestion MALDI-MSI, to investigate the molecular alterations underlying tumor progression, and aid the accurate diagnosis and grading of MLS tumors.

6.2 Methodology

6.2.1 Chemicals and reagents

All chemicals were purchased from Sigma-Aldrich (Steinheim, Germany) except ethanol and xylene (Merck, Darmstadt, Germany). Recombinant Peptide *N*-Glycosidase F (PNGase F) from Flavobacterium meningosepticum was expressed and purified as previously described (Powers et al., 2013).

Table 6-1: Overview of tissue specimens present on the MLS TMA.

TMA		Total	MYX	INT	RC
No. samples		37	23	20	9
No. of patients		32	23	20	9
Gender	*Male vs. Female*	18 vs. 14	14 vs. 9	11 vs. 9	5 vs. 4
Age	*Median [years]*	43	42	43	46
Recurrence		5	3	3	0
Metastasis		4	0	1	1

6.2.2 Tissues, TMA construction and patient grouping

A tissue microarray (TMA) was previously constructed from formalin-fixed, paraffin-embedded (FFPE) MLS tissues from 32 patients diagnosed in the Leiden University Medical Center (Endo et al., 2015; de Graaff et al., 2017). The array consists of 141 needle core biopsies with a 1.5 mm diameter, divided in two paraffin blocks, here referred to as MLS-1 and MLS-2. Both blocks contain an additional six control cores, originating from human placenta, colon, spleen, neuronal, lung, and tonsil tissues. Cores were obtained from three distinct morphological regions in the tumor, myxoid (MYX) areas, intermediate (INT) areas, and round cell (RC) areas. If a patient presented only a single morphology three needle cores were included in the TMA; if more than one morphology was present (MYX+INT, MYX+RC, or INT+RC) two cores per morphology were included. An overview of the TMA is reported in Table 6-1. All samples were handled following the ethical guidelines described in the "Code for Proper Secondary Use of Human Tissue in the Netherlands" of the Dutch Federation of Medical Scientific Societies.

6.2.3 *N*-glycan MALDI-MSI

Both TMA blocks were sectioned using a microtome. 6 µm thick sections were mounted on indium tin-oxide (ITO) coated glass slides (Bruker Daltonics, Bremen, Germany), additionally coated with poly-L-lysine for better adhesion of the needle cores. Importantly, TMA sections were not transferred to the glass slide using a tape transfer system due to the risk of polymer contamination. Slides were dried overnight at 37°C, and stored at 4°C in the dark until further processing. Sample preparation for the on-tissue digestion with PNGase F was performed as previously described (Heijs et al., 2016). *N*-glycan MALDI-MSI analysis was performed using a Bruker RapifleX MALDI-TOF/TOF instrument (Bruker Daltonics). Data was recorded in reflectron, positive-ion mode covering the mass range between *m/z* 900-3,200, using 500 laser shots per spot and a 50 x 50 µm pixel size.

6.2.4 Histology staining and annotation

Following MALDI-MSI analysis, excess MALDI matrix was removed with two ethanol washes (70%, 2x 1min), and the TMA's stained with haematoxylin and eosin (H&E) following routine pathology procedures. The H&E stained TMA's were then scanned using a digital slide scanner (IntelliSite Pathology Ultra-Fast Scanner, Philips, Eindhoven, The Netherlands). The scanned histology images were co-registered to the MALDI-MSI data in flexImaging 5.0 (Bruker Daltonics). In order to obtain a more accurate cellular specificity, the individual TMA cores were annotated by an expert pathologist (JVMGB). The annotations account for intra-core heterogeneity and differentiate between myxoid (MYX), intermediate (INT), and round cell (RC) areas (Figure 6-1). Intermediate areas were more cellular than low grade myxoid areas, but contained too much myxoid matrix to be considered as round cell areas (JVMGB). A total of 157 regions of interest (ROIs) were annotated from the 141 MLS cores.

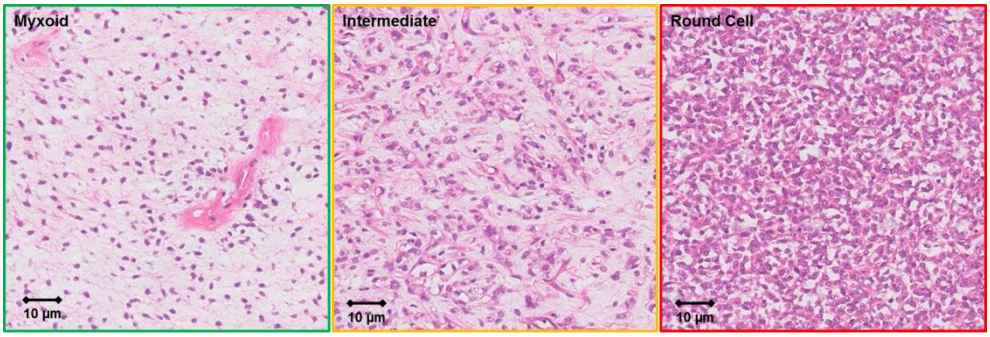

Figure 6-1: Example H&E images of the myxoid, intermediate and round cell areas.

6.2.5 Data pre-processing – *N*-glycans

A TIC normalized average spectrum for each of the 157 annotated ROIs was exported in CSV file format using flexImaging 5.0. Spectral processing, analyte extraction and analyte curation was performed using MassyTools (version 0.1.8.1) (Jansen et al.,

2015). In MassyTools a recalibration of all ROI spectra was performed on the basis of a predefined list of calibrants. Spectra with at least four calibrants (Table S6-1, Supplementary information) with a signal-to-noise (S/N) ratio over nine were considered for further analysis, this resulted in the exclusion of one spectrum. Feature extraction of 115 previously identified *N*-glycans (Heijs et al., 2016; Holst et al., 2016) was performed through integration of the areas of 95% of the theoretical isotopic envelope. A feature specific baseline correction was performed by subtracting the baseline detected within a window of 20 *m/z*. MassyTools additionally included information on the fraction of the analyte area above S/N 9, highest isotope S/N, the mass error per analyte in ppm (averaged for all spectra), as well as a value representing the similarities between the analyzed and theoretical isotope patterns for each analyte (QC, averaged for all spectra). Two spectra were excluded as the "fraction of the analyte area above S/N 9" was below three standard deviations of the mean. The relative areas of a total of 34 *N*-glycans with an average mass error below 30 ppm, and a QC value below 0.4 were rescaled to 100% and considered for the subsequent statistical analysis.

6.2.6 Data analysis

A statistical comparison of the different morphological MLS subtypes (MYX, INT, RC) was performed in MatLab (R2017a, Mathworks, Natick, MA, USA), to find molecular features correlated with tumor progression. The average baseline corrected, relative area for each of the 34 *N*-glycans was calculated for each subtype and for all patients. An Anderson-Darling normality test (adtest) was performed to test the distribution for each of the 34 variables. Variables that did not follow a normal distribution were log-transformed (LOG10) in Microsoft Excel 2010, and retested for normality. A one-way ANOVA analysis (anova1) was used to compare the means of each morphological subtype (p-value < 0.05) for the normally distributed variables. The remaining, non-normally distributed variables were tested using a non-parametric ANOVA (Kruskal-Wallis, kruskalwallis) (p-value < 0.05). Paired tests (Wilcoxon signed rank, signrank) were applied for the comparisons between individual morphological classes (Myx vs. Int, Myx vs. RC, and Int vs. RC). All reported p-values were corrected for multiple testing using the Benjamini-Hochberg test for multiple testing (q-value < 0.05).

6.3 Results & discussion

Grading of MLS patients involves the determination of the round cell component of the tumor. If the round cell component is larger than 5% the patient is considered high grade, as an increased round cell component is associated with poor prognosis (Fletcher et al., 2013; de Graaff et al., 2016; Lemeur et al., 2015; Nishida et al., 2010). In this study we investigated whether MALDI-MSI of *N*-glycans could elucidate diagnostic molecular markers associated with the progression of MLS.

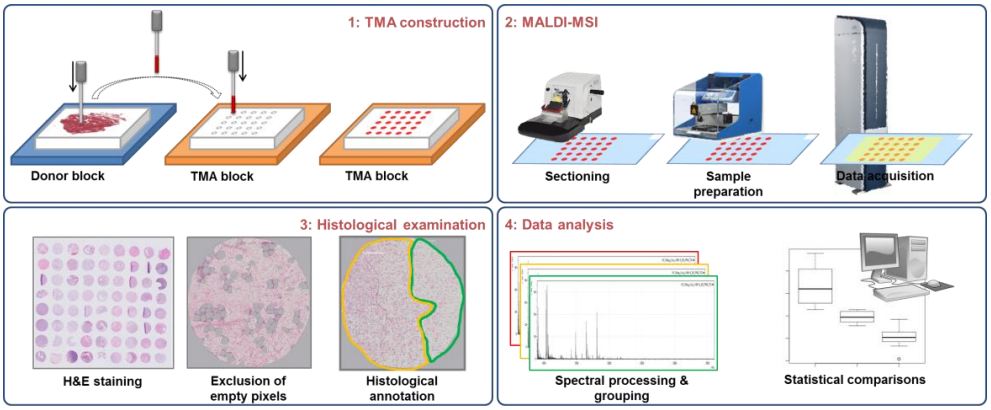

Figure 6-2: Schematic overview of the applied workflow. (1) TMA construction was performed as described in the methodology section, (2) MALDI-MSI of *N*-glycans, (3) histological examination and annotation, and (4) data analysis consisted of processing, grouping of average ROI spectra, and statistical testing.

6.3.1 *N*-glycan MALDI-MSI

The TMA was analyzed by on-tissue digestion MALDI-MSI to characterize the *N*-glycan composition of MLS. 34 *N*-glycans were detected and identified from the MALDI-TOF-MSI dataset. Their respective relative areas were submitted to an ANOVA test to find morphology-associated differences (Figure 6-2&3), Table 6-2). After applying a multiple testing correction five *N*-glycans were significantly associated with morphological changes in MLS (Table 6-2, Figure 6-4), four of which were high-mannose type (H6N2, *m/z* 1419.48 $[M+Na]^+$; H7N2, *m/z* 1581.53 $[M+Na]^+$; H8N2, *m/z* 1743.58 $[M+Na]^+$; H9N2, *m/z* 1905.63 $[M+Na]^+$, where H = Hexose, and N = *N*-acetylhexosamine). Although the sample numbers are small (Table 6-1, MYX vs. INT, n = 14; MYX vs. RC, n = 4; and INT vs. RC, n = 5) hampering paired statistical comparisons and linear regression analysis, there is a clear trend showing elevated levels of high-mannose

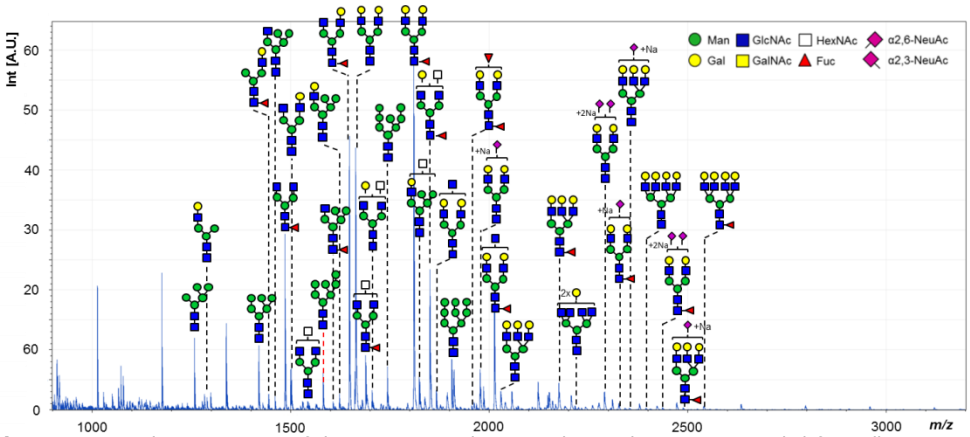

Figure 6-3: Visual representation of the MLS TMA *N*-glycan MSI basepeak spectrum compiled from all MLS cores present on the TMA. The spectrum represents the TMA's total *N*-glycan content and includes the 34 annotated *N*-glycans and their assigned compositions.

glycans with MLS tumor progression (Table 6-2 & S6-2, Supplementary information) (Figure 6-4A,B,C,D). Similarly, the association between high-mannose type glycans and tumor progression was previously described for breast cancer, ovarian cancer, and colorectal cancers (Anugraham et al., 2014; Kaprio et al., 2015; Leoz et al., 2011; Liu et al., 2013). The exact role of high-mannose glycans in cancer is still unknown. However, their higher abundance has been hypothesized to be an effect of reduced or incomplete maturation during the protein glycosylation pathway (Holst et al., 2015; Zhao et al., 2008). High-mannose type glycans can occur both intracellular and on the cell surface. During *N*-glycan biosynthesis on the surface of the cytoplasmic side of the endoplasmatic reticulum (ER), lipid-linked oligosaccharide precursors (LLO) are produced, containing up to five mannose residues. Once the LLO contains five mannose residues it moves to the ER lumen where an additional 4 mannose and 3 glucose residues are added. Upon completion, the glycan is transferred to its protein carrier and the glucose and mannose residues are trimmed resulting in the production of protein-bound high-mannose type glycans. The high-mannose glycosylated proteins will either be transferred to the cell- surface or to the Golgi apparatus for further processing in to complex- or hybrid-type *N*-glycans (Freeze, 2006). In normal cells, high-mannose type glycans play a crucial role in both protein folding and the protection of proteins against degradation during intracellular relocalization. The hypothesis of an increased abundance of high-mannose glycans caused by a disruption of the biosynthesis pathway or through reduced expression of mannosidases is very plausible. The MALDI-MSI experiments were not performed with the spatial resolution needed to distinguish between intra- or extracellular *N*-glycans; microscopic analysis of tissues immuno-stained with high-mannose-binding antibodies, like Concanavalin A, could be performed to provide additional information on the subcellular location of the high-mannose glycans, although it is not solely specific for high-mannose type glycans and was beyond the scope of this study.

The other *N*-glycan that displayed significant differences between the three morphological groups was a monofucosylated, monosialylated tri-antennary complex-type glycan (H6N5F1S1, *m/z* 2487.85 $[M+Na]^+$, where F = fucose, and S = *N*-acetylneuraminic acid) (Figure 6-4E). It should be noted that the *N*-glycans, and more specifically the sialic acids, were not derivatized prior to the MALDI-MSI analysis. Sialic acids are highly labile groups, frequently lost during the MALDI-MS analysis, and so represents a detection bias against sialylated *N*-glycan species (Holst et al., 2016). Like the high-mannose type glycans, the abundance of the triantennary complex type glycan shows a positive correlation with tumor progression. The increased β1,3- and β1,6-linked GlcNAc branching of *N*-glycans, caused by an overexpression of the MGAT4 and MGAT5 genes which are coding for *N*-acetylglucosaminyltransferase IV (GnT-IV) and *N*-acetylglucosaminyltransferase V (GnT-V), has been previously associated with invasion and metastasis in breast and colorectal cancer (D'Arrigo et al., 2005; Dennis et al., 1987, 1999; Fernandes et al., 1991). Overexpression of GnT-V and the resulting

Table 6-2: Kruskal-Wallis results for the morphological comparison. Compositions legend: H = Glc/Gal/HexNAc, N = Man/Gal, F = Fucose, S = NeuAc. Sialic acids (S) were detected in their sodium salt form. P-values and q-values < 0.05 are highlighted in green.

Composition	m/z	QC value	Error	Relative areas MYX			INT			RC			Statistics Kruskal-Wallis	ANOVA	Benjamini-Hochberg
	[M+Na]+	A.U.	ppm	Median	Q1	Q2	Median	Q1	Q2	Median	Q1	Q2	p-value	p-value	q-value
H5N2	1257.42	0.03	3.43	0.2269	0.0810	0.3798	0.2316	0.1360	0.3877	0.4252	0.1964	0.5181		0.2203	0.6247
H4N3	1298.45	0.29	17.87	-0.1321	-0.1714	-0.0864	-0.1090	-0.1690	-0.0790	-0.1628	-0.2390	-0.0141		0.5694	0.8840
H6N2	1419.48	0.04	2.28	2.3224	1.9771	2.5792	2.4980	2.2434	2.8684	3.0039	2.5097	3.8470		0.0066	0.0170
H4N3F1	1444.51	0.11	11.73	0.6509	0.5904	0.7310	0.6659	0.5742	0.7493	0.6228	0.5346	0.7151		0.7465	0.9380
H5N3	1460.50	0.09	13.58	0.4876	0.3822	0.6478	0.5019	0.4472	0.6437	0.5782	0.4651	0.7713		0.5941	0.9380
H3N4F1	1485.53	0.03	2.37	0.8305	0.6438	0.9138	0.7425	0.5883	0.9240	0.8273	0.6503	0.8987		0.6721	0.9380
H4N4	1501.53	0.12	8.91	2.0870	1.8289	2.3192	1.9762	1.7407	2.1993	1.8632	1.6050	2.1815		0.4798	0.9380
H3N5	1542.56	0.29	14.69	-0.2449	-0.3801	-0.1456	-0.2963	-0.3663	-0.1789	-0.2742	-0.3184	-0.2168		0.8896	0.9499
H7N2	1581.53	0.06	5.13	0.1651	0.0798	0.2870	0.2358	0.1525	0.3064	0.3395	0.2707	0.4968		0.0070	0.0476
H5N3F1	1606.56	0.22	26.79	0.5038	0.3228	0.6572	0.5610	0.3785	0.7181	0.5646	0.4894	0.6965		0.4651	0.9380
H6N3	1622.55	0.14	13.76	0.7664	0.5456	1.0289	0.7609	0.5347	0.9910	0.8253	0.5731	1.0335		0.6733	0.9380
H4N4F1	1647.59	0.02	2.62	14.2666	11.5159	15.3986	11.8450	9.6574	13.8976	10.7546	8.9886	13.0586		0.2182	0.7388
H5N4	1663.58	0.11	7.10	13.6345	10.2220	17.4224	14.2730	10.7191	15.7761	12.7201	11.0405	15.1622		0.9534	0.9499
H3N5F1	1688.61	0.22	3.43	0.4430	0.3860	0.5719	0.4828	0.3735	0.5312	0.4910	0.4325	0.5528		0.9348	0.9499
H4N5	1704.61	0.19	7.59	-0.0025	-0.0514	0.1585	0.0168	-0.0666	0.1263	0.0571	-0.0322	0.0852		0.6879	0.9380
H8N2	1743.58	0.03	6.56	0.1782	-0.0111	0.3398	0.2399	0.1421	0.3811	0.4138	0.3592	0.5848		0.0043	0.0374
H5N4F1	1809.64	0.05	2.40	17.2096	15.7826	20.8344	17.6100	16.0625	19.5415	15.4246	12.9683	17.4112		0.2203	0.6147
H6N4	1825.63	0.13	16.04	1.1434	1.0673	1.2882	1.3642	1.1535	1.7781	1.2466	1.2039	1.3582	0.1403		0.5963
H4N5F1	1850.67	0.04	2.77	5.5834	4.9093	10.2248	6.0127	4.8494	10.0062	5.3689	5.0601	7.9270	0.9135		0.9499
H5N5	1866.66	0.07	5.01	-0.0215	-0.0619	0.0599	0.0145	-0.1136	0.1307	-0.0219	-0.1170	0.0205		0.7860	0.9499
H9N2	1905.63	0.03	4.24	0.3102	0.1368	0.4059	0.4010	0.2838	0.5001	0.5935	0.4693	0.7681		0.0038	0.0374
H5N4F2	1955.70	0.17	8.49	-0.6903	-0.8110	-0.6225	-0.7385	-0.8154	-0.5830	-0.7611	-0.8803	-0.5459		0.4803	0.9380
H5N4S1	1976.66	0.10	5.24	2.8883	1.8839	3.4559	2.7699	1.9896	3.3792	2.2893	2.2435	2.9301		0.8917	0.9499
H5N5F1	2012.72	0.05	2.56	6.8598	4.9867	9.0870	8.0536	4.4595	10.9335	5.7821	4.7750	7.5416		0.8236	0.9499
H6N5	2028.71	0.18	7.47	0.2195	0.0567	0.2508	0.1970	0.0650	0.2777	0.1614	0.0877	0.2667		0.8837	0.9499
H6N5F1	2174.77	0.14	5.81	0.2463	0.1811	0.3292	0.3065	0.2350	0.4063	0.3842	0.2689	0.4538		0.0664	0.3225
H5N6F1	2215.80	0.15	9.89	0.1548	0.0840	0.3669	0.3886	0.1223	0.4872	0.2675	0.2048	0.5149	0.1808		0.6147
H5N4S2	2289.74	0.16	9.12	1.6829	0.9493	2.1357	1.6612	1.2861	1.8581	1.4698	1.1300	1.9194		0.9921	0.9499
H5N5F1S1	2325.80	0.17	18.10	-0.2408	-0.2924	-0.1567	-0.1773	-0.2460	-0.1450	-0.1636	-0.1767	-0.1124		0.2590	0.7315
H6N5S1	2341.79	0.25	15.16	0.2053	0.1455	0.2498	0.2051	0.1720	0.2779	0.2111	0.1586	0.2734		0.6251	0.9380
H7N6	2393.85	0.31	15.99	-0.7508	-0.8184	-0.6058	-0.6531	-0.7307	-0.5791	-0.6932	-0.7169	-0.5632		0.2797	0.7315
H5N4F1S2	2435.79	0.28	16.89	0.2190	0.1567	0.2851	0.2244	0.1857	0.2631	0.2727	0.2239	0.3027		0.3157	0.8183
H6N5F1S1	2487.85	0.27	24.40	-0.7168	-0.8005	-0.6704	-0.6365	-0.7398	-0.5638	-0.5717	-0.6219	-0.4783		0.0044	0.0374
H7N6F1	2539.90	0.19	20.69	-0.5305	-0.6061	-0.4418	-0.3653	-0.5547	-0.3034	-0.3346	-0.4403	-0.3188		0.0234	0.1326

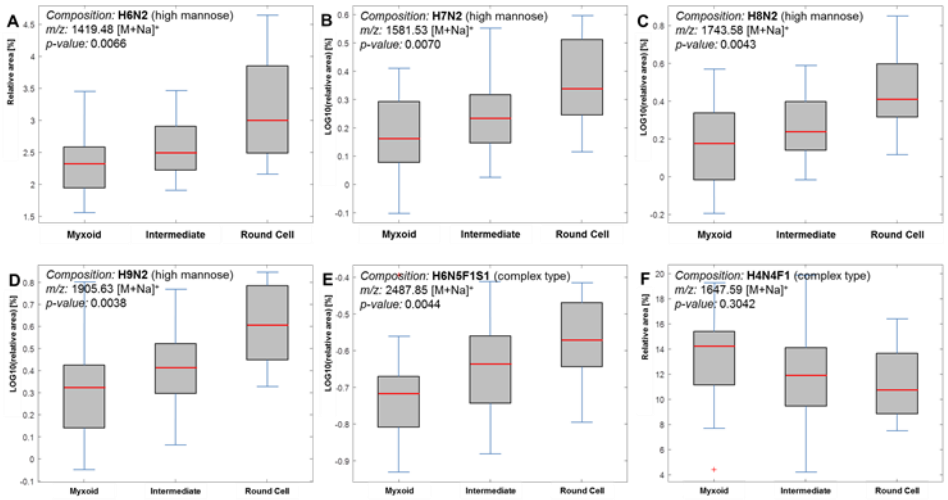

Figure 6-4: (A-E) Boxplots displaying the relative area distributions of the five *N*-glycans with significant variance between the three morphological classes. (F) Boxplot displaying the relative area distributions of a monofucosylated bi-antennary complex type *N*-glycan.

increase in *N*-glycans with extended β1,6-linked GlcNAc branching, resulted in an increased cell motility, a loss of contact inhibition, and caused morphological transformation of normal human epithelial cells (Demetriou et al., 1995; Holst et al., 2015). Additionally, mice with a MGAT5 deficiency showed a suppression of mammary tumor cell growth and metastasis (Granovsky et al., 2000; Holst et al., 2015). The increased activity of GnT-V is also believed to result in a complementary decrease in biantennary complex type *N*-glycans (Dennis et al., 1987). Although not statistically significant, the presented results show a similar trend (Figure 6-4F, Table 6-2). While little is known about glycosylation changes in MLS, these previous findings would support a role for *N*-glycans in tumor progression in MLS. The biosynthesis of complex-type *N*-glycans is dependent on the activity of a large number of different glycosyltransferases, changes in the expression of these enzymes result in changed glycosylation profiles. The increased abundance of complex-type glycans indicates that the maturation of glycans is not completely disrupted, as this would primarily result in an increased abundance of high-mannose-type glycans and truncated glycans. Expression analysis of the genes coding for the various glycosyltransferases, or a quantitative (micro)proteomics approach, could help identify which enzymes cause the altered glycosylation profiles in the different MLS grades. While the presented results clearly display a positive correlation between the abundance of several *N*-glycans and the progression of MLS (Figure 6-4A-E), a potential complicating factor is that MLS tumor progression is associated with an increase in cellularity (Fletcher et al., 2013). The majority of the glycoproteins are either secreted or membrane-bound. The *N*-glycans analyzed by MALDI-MSI are no longer attached to their carrier proteins, which makes it impossible to establish whether a glycan was bound to a membrane protein or

a secreted, extracellular protein. Correcting for cell density may correct for contribution from membrane-bound proteins, but would introduce a bias for secreted proteins. Importantly the changed glycan profile reported here for MLS shows a clear correlation with previously published work performed on cell lines in which the number of cells were monitored and the results normalized (Demetriou et al., 1995) indicating that the changed glycan profile represents a biological effect, such as the overexpression of GnT-V causing the increase in β1,6-linked GlcNAc branching, or the reduced expression of mannosidases causing the increase in high-mannose-type glycans, rather than an artifact due to differences in cell density.

6.4 Conclusions

The presented results indicate an association between the increase of high-mannose-type *N*-glycans and a triantennary complex-type glycan with progression of MLS. Additional protein and lipid MSI studies, as well as an in-depth analysis of the proteome should shed light on the nature of these molecular alterations.

6.5 Acknowledgements

This work was supported by the ZonMW Zenith project "Imaging Mass Spectrometry-Based Molecular Histology: Differentiation and Characterization of Clinically Challenging Soft Tissue Sarcomas" (No. 93512002; B.H.), and the Liddy Shriver Sarcoma Initiative. The authors would like to thank Dr. Sarantos Kostidis for his valuable input and Prof. dr. Richard Drake and dr. Anand Mehta for kindly producing and providing the PNGase F required for this study.

6.6 Supplementary information

6.6.1 Supplementary tables

Table S6-1: Glycan compositions used as calibrants. Compositions legend: H = Glc/Gal/HexNAc, N = Man/Gal, F = Fucose.

Composition	***m/z*** $[M+Na]^+$
H5N2	1257.42
H3N4F1	1485.53
H4N4F1	1647.58
H5N4F1	1809.64
H5N5F1	2012.72

Table S6-2: Wilcoxon signed rank test results for the morphological comparison. Compositions legend: H = Glc/Gal/HexNAc, N = Man/Gal, F = Fucose, S = NeuAc (as sodiated species). P-values and q-values < 0.05 are highlighted in green.

Composition	***m/z***	**Myx vs Int (**n = 11)		**Myx vs RC (**n = 4)		**Int vs RC (**n = 5)	
	$[M+Na]^+$	*p-value*	*q-value*	*p-value*	*q-value*	*p-value*	*q-value*
H6N2	1419.48	0.5830	0.7212	0.2500	0.4688	0.6250	0.7212
H7N2	1581.53	0.3575	0.5959	0.2500	0.4688	0.1875	0.4688
H8N2	1743.58	0.5416	0.7212	0.1250	0.4688	0.1250	0.4688
H9N2	1905.63	0.7609	0.8152	0.2500	0.4688	0.1875	0.4688
H6N5F1S1	2487.85	0.0017	0.0256	1.0000	1.0000	0.4375	0.6563